in the Notch1(11–13)–DLL4$_{SLP}$(N-EGF2) complex to clarify their effect on receptor binding (fig. S7B) (*39*). The majority of AGS mutations are predicted to disrupt disulfide bond formation, perturb the hydrophobic core of the MNNL domain, or interfere with inter-EGF packing. However, mutations at conserved Thr^{110} and Tyr^{179} residues would directly affect binding, whereas other mutations at Gly^{28}, Pro^{112}, and Val^{151} positions could indirectly influence interactions by distorting the MNNL-DSL linker (fig. S7B). Notably, one AGS patient had a Jagged1 mutation analogous to the DLL4 G28S mutation isolated from our affinity maturation experiments, raising the possibility that the mutation disrupts Notch binding in the context of Jagged1 (fig. S7B) (*40*).

Implications for therapeutic targeting of the Notch pathway

The distinct pathologies linked to Notch receptors and ligands necessitates the development of more precisely targeted therapies. For example, Notch1 mutations are associated with leukemia and aortic valve disease, Notch3 mutations with cerebral autosomal dominant arteriopathy with subcortical infarcts and leukoencephalopathy, and Jagged1/Notch2 mutations with AGS (*39*, *41*–*44*). Physiological processes can also be differentially regulated by ligands, evidenced by the opposing roles of Jagged1 and DLL4 in angiogenesis and the role of the Notch1-DLL4 axis in lymphatic development and the lymphatic system (*45*, *46*). Certain advantages of receptor-specific therapeutics have begun to emerge in studies describing the inhibition of tumor growth by Notch1-antagonist antibodies and the control of graft-versus-host disease by DLL1/4-antagonist antibodies (*47*, *48*). The Notch1(11–13)–DLL4$_{SLP}$(N-EGF1) structure provides new insights toward the development of receptor- and ligand-specific drugs. Antibodies against Notch EGF11 and 12 reportedly have limited effectiveness in cellular assays; based on the structure, this is likely due to occlusion of relevant protein epitopes by the Ser^{435} O-glucose and Thr^{466} O-fucose moieties (*49*). More effective therapeutic targeting of EGF11 and 12 may be achieved with engineered high-affinity ligands such as those presented here, which have coevolved with Notch receptors to accommodate O-glycan binding.

REFERENCES AND NOTES

1. S. Artavanis-Tsakonas, M. D. Rand, R. J. Lake, *Science* **284**, 770–776 (1999).
2. L. A. Milner, A. Bigas, *Blood* **93**, 2431–2448 (1999).
3. Y. Nyfeler *et al.*, *EMBO J.* **24**, 3504–3515 (2005).
4. F. Radtke, H. R. MacDonald, F. Tacchini-Cottier, *Nat. Rev. Immunol.* **13**, 427–437 (2013).
5. R. J. Fleming, *Semin. Cell Dev. Biol.* **9**, 599–607 (1998).
6. G. Struhl, I. Greenwald, *Nature* **398**, 522–525 (1999).
7. B. De Strooper *et al.*, *Nature* **398**, 518–522 (1999).
8. C. Brou *et al.*, *Mol. Cell* **5**, 207–216 (2000).
9. W. R. Gordon *et al.*, *Nat. Struct. Mol. Biol.* **14**, 295–300 (2007).
10. E. M. Hansson, U. Lendahl, G. Chapman, *Semin. Cancer Biol.* **14**, 320–328 (2004).
11. M. Acar *et al.*, *Cell* **132**, 247–258 (2008).
12. T. Okajima, K. D. Irvine, *Cell* **111**, 893–904 (2002).
13. P. Taylor *et al.*, *Proc. Natl. Acad. Sci. U.S.A.* **111**, 7290–7295 (2014).
14. C. Hicks *et al.*, *Nat. Cell Biol.* **2**, 515–520 (2000).
15. V. M. Panin, V. Papayannopoulos, R. Wilson, K. D. Irvine, *Nature* **387**, 908–912 (1997).
16. J. Chen, D. J. Moloney, P. Stanley, *Proc. Natl. Acad. Sci. U.S.A.* **98**, 13716–13721 (2001).
17. C. Y. Janda, D. Waghray, A. M. Levin, C. Thomas, K. C. Garcia, *Science* **337**, 59–64 (2012).
18. J. Cordle *et al.*, *Nat. Struct. Mol. Biol.* **15**, 849–857 (2008).
19. C. R. Chillakuri *et al.*, *Cell Reports* **5**, 861–867 (2013).
20. I. Rebay *et al.*, *Cell* **67**, 687–699 (1991).
21. M. B. Andrawes *et al.*, *J. Biol. Chem.* **288**, 25477–25489 (2013).
22. S. Yamamoto *et al.*, *Science* **338**, 1229–1232 (2012).
23. B. D'Souza, A. Miyamoto, G. Weinmaster, *Oncogene* **27**, 5148–5167 (2008).
24. P. Whiteman *et al.*, *J. Biol. Chem.* **288**, 7305–7312 (2013).
25. C. Hicks *et al.*, *J. Neurosci. Res.* **68**, 655–667 (2002).
26. J. T. Nichols *et al.*, *J. Cell Biol.* **176**, 445–458 (2007).
27. R. G. Fehon *et al.*, *Cell* **61**, 523–534 (1990).
28. J. F. de Celis, S. Bray, *Development* **124**, 3241–3251 (1997).
29. D. Sprinzak *et al.*, *Nature* **465**, 86–90 (2010).
30. J. Cordle *et al.*, *J. Biol. Chem.* **283**, 11785–11793 (2008).
31. S. Hambleton *et al.*, *Structure* **12**, 2173–2183 (2004).
32. E. Ladi *et al.*, *J. Cell Biol.* **170**, 983–992 (2005).
33. N. A. Rana, R. S. Haltiwanger, *Curr. Opin. Struct. Biol.* **21**, 583–589 (2011).
34. R. Rampal, J. F. Arboleda-Velasquez, A. Nita-Lazar, K. S. Kosik, R. S. Haltiwanger, *J. Biol. Chem.* **280**, 32133–32140 (2005).
35. J. A. Porter, K. E. Young, P. A. Beachy, *Science* **274**, 255–259 (1996).
36. A. Xu, L. Lei, K. D. Irvine, *J. Biol. Chem.* **280**, 30158–30165 (2005).
37. W. D. Morgan *et al.*, *J. Mol. Biol.* **289**, 113–122 (1999).
38. W. Held, R. A. Mariuzza, *Nat. Rev. Immunol.* **8**, 269–278 (2008).
39. N. B. Spinner *et al.*, *Hum. Mutat.* **17**, 18–33 (2001).
40. D. M. Warthen *et al.*, *Hum. Mutat.* **27**, 436–443 (2006).
41. A. P. Weng *et al.*, *Science* **306**, 269–271 (2004).
42. V. Garg *et al.*, *Nature* **437**, 270–274 (2005).
43. A. Joutel *et al.*, *Nature* **383**, 707–710 (1996).
44. R. McDaniell *et al.*, *Am. J. Hum. Genet.* **79**, 169–173 (2006).
45. R. Benedito *et al.*, *Cell* **137**, 1124–1135 (2009).
46. K. Niessen *et al.*, *Blood* **118**, 1989–1997 (2011).
47. Y. Wu *et al.*, *Nature* **464**, 1052–1057 (2010).
48. I. T. Tran *et al.*, *J. Clin. Invest.* **123**, 1590–1604 (2013).
49. R. Falk *et al.*, *Methods* **58**, 69–78 (2012).

ACKNOWLEDGMENTS

We thank A. Velasco, D. Waghray, and J. Spangler for assistance. We also thank the staff of the Advanced Photon Source for support and access to the 23-ID-D beamline; the staff of the Advanced Light Source for support and access to the 8.2.2 Howard Hughes Medical Institute (HHMI) beamline; and the staff of the Stanford Synchrotron Radiation Lightsource, which is supported by the U.S. Department of Energy, Office of Science, Office of Basic Energy Sciences under contract DE-AC02-76SF00515. This work was supported by NIH-1RO1-GM097015, Ludwig Cancer Foundation, and the HHMI (K.C.G.). V.C.L. was supported by a Cancer Research Institute postdoctoral fellowship and an NIH-Immunology postdoctoral training grant. M.V.N. was supported by the Stanford Discovery Innovation fund, and N.W.P. was supported by an HHMI fellowship of the Helen Hey Whitney Foundation. K.C.G. and V.L. are inventors on a patent applied for by Stanford University describing high-affinity Notch ligands. Coordinates and structure factors of 1egf DLL4 and 2egf DLL4 have been deposited in the Protein Data Bank with accession codes 4XL1 and 4XLW.

SUPPLEMENTARY MATERIALS

www.sciencemag.org/content/347/6224/847/suppl/DC1
Materials and Methods
Supplementary Text
Figs. S1 to S9
Tables S1 to S2
References (*50*–*65*)

10 September 2014; accepted 14 January 2015
10.1126/science.1261093

REPORTS

QUANTUM ENGINEERING

Confining the state of light to a quantum manifold by engineered two-photon loss

Z. Leghtas,[1]* S. Touzard,[1] I. M. Pop,[1] A. Kou,[1] B. Vlastakis,[1] A. Petrenko,[1] K. M. Sliwa,[1] A. Narla,[1] S. Shankar,[1] M. J. Hatridge,[1] M. Reagor,[1] L. Frunzio,[1] R. J. Schoelkopf,[1] M. Mirrahimi,[2,1] M. H. Devoret[1]

Physical systems usually exhibit quantum behavior, such as superpositions and entanglement, only when they are sufficiently decoupled from a lossy environment. Paradoxically, a specially engineered interaction with the environment can become a resource for the generation and protection of quantum states. This notion can be generalized to the confinement of a system into a manifold of quantum states, consisting of all coherent superpositions of multiple stable steady states. We have confined the state of a superconducting resonator to the quantum manifold spanned by two coherent states of opposite phases and have observed a Schrödinger cat state spontaneously squeeze out of vacuum before decaying into a classical mixture. This experiment points toward robustly encoding quantum information in multidimensional steady-state manifolds.

Stabilizing the state of a system in the vicinity of a predefined state despite the presence of external perturbations plays a central role in science and engineering. On a quantum system, stabilization is a fundamentally more subtle process than on a classical system, as it requires an interaction that, quantum mechanically, is always invasive. The mere act of learning something about a system perturbs it. Carefully designed nondestructive quantum measurements have recently

[1]Department of Applied Physics, Yale University, New Haven, CT 06520, USA. [2]Institut National de Recherche en Informatique et en Automatique (INRIA) Paris-Rocquencourt, Domaine de Voluceau, B.P. 105, 78153 Le Chesnay Cedex, France.
*Corresponding author. E-mail: zaki.leghtas@yale.edu

been incorporated in feedback loops to stabilize a single quantum state (*1*–*4*). Alternatively, adequately engineering an interaction with an auxiliary dissipative system, termed "engineered dissipation," can also stabilize a single quantum state (*5*–*8*).

Can engineered dissipation protect all unknown superpositions of two states, thus protecting quantum information? In fact, the static random access memory of a computer chip dynamically stabilizes the states representing 0 and 1 by combining the energy supply and dissipation, providing fast

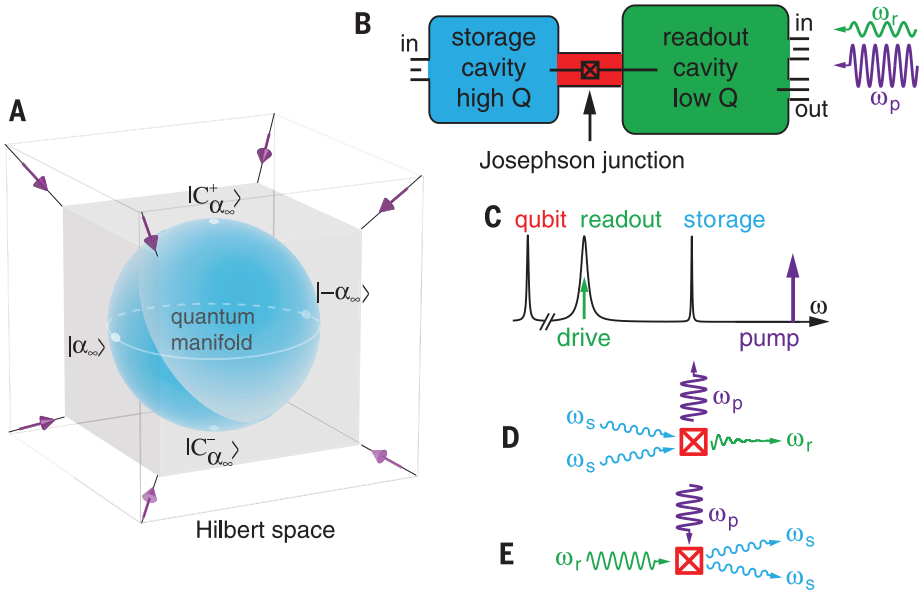

Fig. 1. Schematic of the experiment. (**A**) Confinement of a quantum state belonging to a large Hilbert space into a 2D quantum manifold. The outer and inner cubes form a hypercube representing a multidimensional Hilbert space. The inner blue sphere represents the manifold of states spanned by the two coherent states $|\pm\alpha_\infty\rangle$. Quantum states such as the even and odd Schrödinger cat states $|C^{\pm}_{\alpha_\infty}\rangle = \mathcal{N}(|\alpha_\infty\rangle \pm |-\alpha_\infty\rangle)$ also belong to this manifold, where $\mathcal{N}$ is a normalization factor. Stabilizing forces direct all states toward the inner sphere without inducing any rotation in this subspace, as indicated by the purple arrows. (**B**) Two superconducting cavities are coupled through a Josephson junction. Pump and drive microwave tones are applied to the readout, creating the appropriate nonlinear interaction, which generates a coherent superposition of steady states in the storage. The readout output port is connected to an amplifier chain [(*17*), section 1.2]. Direct Wigner tomography of the storage is performed using its input port and the qubit mode. Q stands for "quality factor." (**C**) Schematic spectrum of different modes involved in the experiment. The pump and drive tones are shown as vertical arrows. (**D** and **E**) Four-wave processes involved in the nonlinear damping and nonlinear drive, respectively, experienced by the storage. In (D), two photons of the storage combine and convert, stimulated by the pump tone, into a readout photon that is irreversibly radiated away by the transmission line. This process is balanced by the conversion of the drive tone, which, in the presence of the pump, creates two photons in the storage (E).

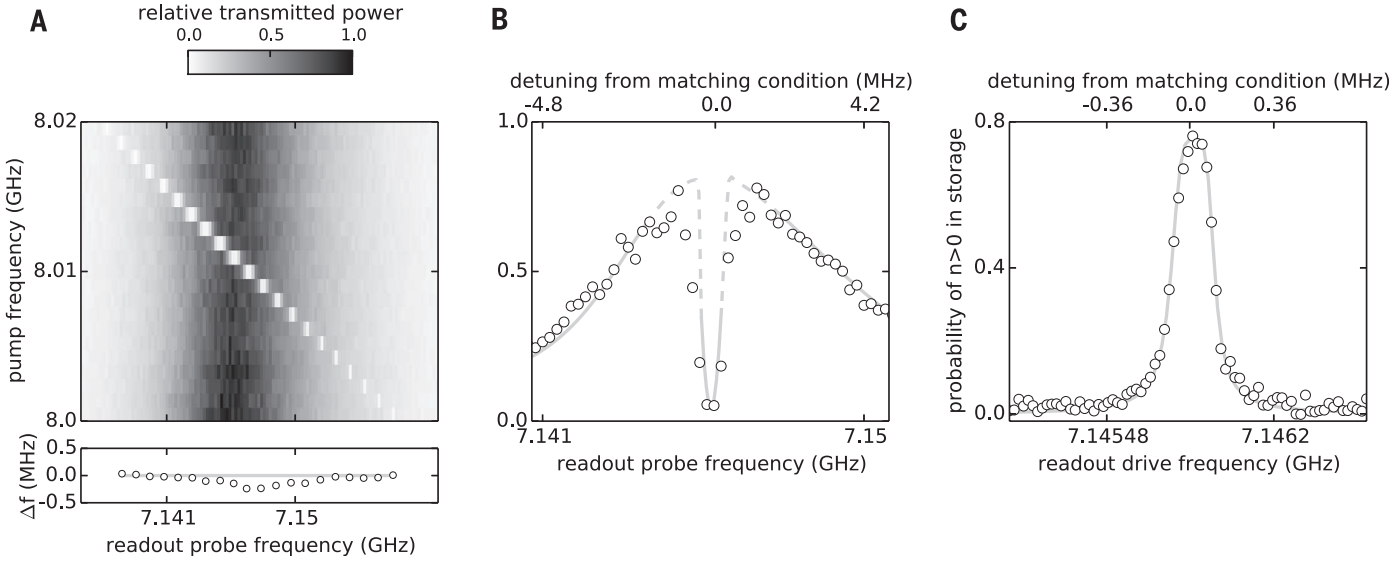

Fig. 2. Conversion of readout photons into pairs of storage photons. (**A** and **B**) CW spectroscopy of the readout in presence of the pump tone. The grayscale represents transmitted power of the probe tone through the readout as a function of probe frequency (horizontal axis) and pump frequency (vertical axis). In the top panel of (A), the usual Lorentzian response develops a sharp and deep dip, signaling conversion of probe photons into storage photons. The dip frequency $\omega_{dip}(\omega_p)$ decreases as the pump frequency increases. In the lower panel of (A), we plot $\Delta f = \omega_{dip}/2\pi - (2\omega_s - \omega_p)/2\pi$ for each dip and see that the deviation of the data (open circles) to the theory (full line: $\Delta f = 0$) is only of the order of 0.24 MHz over a span of 20 MHz. The Stark-shifted value of ω_s due to the pump is used [(*17*), fig. S5]. (B) Cut of the gray-scale map (A) at $\omega_p/2\pi$ = 8.011 GHz. (**C**) Conversion seen from the storage, represented as the probability of not being in the vacuum state, as a function of drive frequency. The dashed and full lines in (B) and (C) are the result of a numerical computation of the steady-state density matrix of the system with Hamiltonian (Eq. 2) and loss operators $\sqrt{\kappa_s}\mathbf{a}_s$, $\sqrt{\kappa_r}\mathbf{a}_r$, sweeping the drive frequency and keeping the pump frequency fixed. All parameters entering in theoretical predictions were measured or estimated independently. However, in (C) the theory was rescaled by a factor of 0.76 to fit the data. We believe that the need for this rescaling is a consequence of the unexplained modified qubit relaxation times when the pump and the drive are on [(*17*), section 1.4.9].

access time and robustness against noise. For a quantum memory, however, the system must not only have one or two stable steady states (SSSs), but rather a whole quantum manifold composed of all coherent superpositions of two SSSs (Fig. 1A). All quantum states are attracted to this manifold and are thus protected against diffusion out of it. However, by construction, such a system does not distinguish between all of its SSSs and hence cannot correct against random transitions within the quantum manifold.

An oscillator that exchanges only pairs of photons with a dissipative auxiliary system (*9*) is a practical example that displays a manifold of SSSs. This two-photon loss will force and confine the state of the oscillator into the quantum manifold spanned by two oscillation states with opposite phases. Uncontrolled energy decay, termed "single-photon loss," causes decoherence within the SSS manifold, and hence quantum superpositions will eventually decay into classical mixtures. Nevertheless, in the regime where pairs of photons are extracted at a rate at least as large as the single-photon decay rate, transient quantum coherence can be observed. This regime requires combining strong nonlinear interactions between modes and low single-photon decay rates.

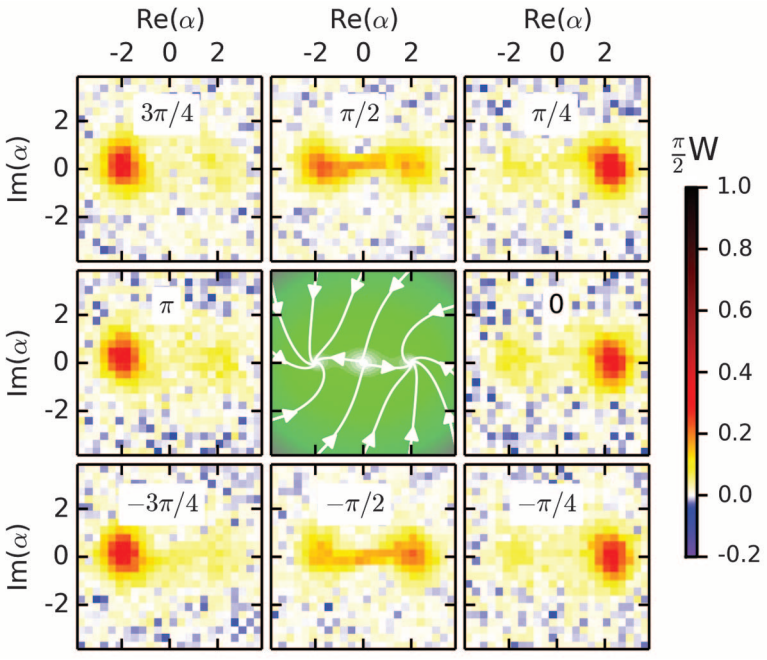

Fig. 3. Bistable behavior of the steady-state manifold of the nonlinearly driven damped storage oscillator. The central panel shows the theoretical classical equivalent of a potential of the storage nonlinear dynamics. The modulus of the velocity (color) has three zeroes corresponding to two SSSs $|\pm\alpha_\infty\rangle$ and the saddle point $|0\rangle$. Trajectories initialized on the panel border converge to one of these two SSSs. These trajectories are curved due to the Kerr effect. The outside panels show the measured Wigner function W(α) of the storage after 10 μs of pumping for different initial states. For each panel, we initialize the storage in a coherent state of amplitude α_k, where $|\alpha_k| = 2.6$ and $\arg(\alpha_k)$ is indicated in each panel. The storage converges to a combination of $|\pm\alpha_\infty\rangle$. The weight of each of these two states and the coherence of their superposition is set by the initial state. For the initial phases $\arg(\alpha_k) = 0, \pm\pi/4$, the storage mainly evolves to $|\alpha_\infty\rangle$, with only a small weight on $|-\alpha_\infty\rangle$. On the other hand, for initial phases $\arg(\alpha_k) = \pm 3\pi/4, \pi$, the state mainly evolves to $|-\alpha_\infty\rangle$, with a small weight on $|\alpha_\infty\rangle$. For the initial phases $\arg(\alpha_k) = \pm\pi/2$, the initial state is almost symmetrically positioned with respect to the two states $|\pm\alpha_\infty\rangle$ and has no definite parity (even and odd photon number states are almost equally populated). Hence, the state evolves to a mixture of $|\pm\alpha_\infty\rangle$. Re(α) and Im(α) denote the real and imaginary part of α, respectively.

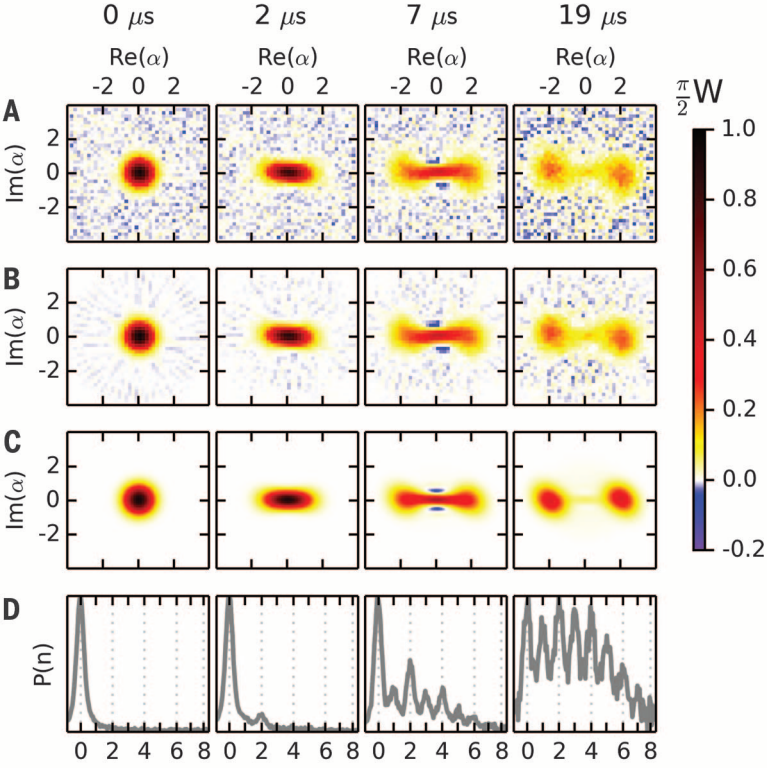

Fig. 4. Time evolution of the storage state in the presence of the nonlinear drive and dissipation processes. The panels correspond to measured data (**A**), reconstructed density matrices (*22*) (**B**), and numerical simulations (**C**). They display the Wigner function after a pumping duration indicated at the top of each column. The storage is initialized in the quantum vacuum state at time $t = 0$ μs. First, the state squeezes in the Q quadrature ($t = 2$ μs). Small but visible negativities appearing at $t = 7$ μs indicate that the superposition of the SSSs shown in Fig. 3 is now coherent and that a continuous evolution from a squeezed state to a quantum state approximating a Schrödinger cat state is taking place. Finally, these negativities disappear as a consequence of the unavoidable storage photon loss, and the state decays into a statistical mixture of the two SSSs ($t = 19$ μs). (**D**) Storage photon number distribution P(n) measured using the photon number splitting of the qubit (*29*). At $t = 2{,}7$ μs, the $n = 2$ population is larger than $n = 1$. A similar population inversion is also present between $n = 4$ and $n = 3$ at $t = 7$ μs. The non-Poissonian character of the photon number distribution at $t = 2{,}7$ μs confirms the nonclassical nature of the dynamical states of the storage for these intermediate times.

Our experiment enters this regime and demonstrates transient quantum states through a circuit quantum electrodynamics architecture (*10*), benefiting from the strong nonlinearity and low loss of a Josephson junction. Our setup (Fig. 1B), based on a recent proposal (*11*), consists of two superconducting microwave oscillators coupled through a Josephson junction in a bridge transmon configuration (*12*). These oscillators are the fundamental modes of two superconducting cavities. One cavity, termed "the storage," holds the manifold of SSSs and is designed to have minimal single-photon dissipation. The other, termed "the readout," is overcoupled to a transmission line, and its role is to evacuate entropy from the storage. In a variety of nonlinear systems, the interaction of a pump tone with relevant degrees of freedom provides cooling (*13*), squeezing (*14*), and amplification (*15*, *16*). Similarly, we use the four-wave mixing capability of the Josephson junction to generate a coupling that exchanges pairs of photons in the storage with single photons in the readout.

By off-resonantly pumping the readout at an angular frequency

$$\omega_p = 2\omega_s - \omega_r \quad (1)$$

where ω_r and ω_s are the readout and storage angular frequencies, respectively, the pump stimulates the conversion of two storage photons into one readout photon and one pump photon. The readout photon then rapidly dissipates through the transmission line, resulting in a loss in photon pairs for the storage (Fig. 1D). This engineered dissipation is the key ingredient in our experiment. The input power that balances this dissipation is provided by the readout drive, a weak resonant irradiation of the readout. Due to the nonlinear mixing with the pump, these input readout photons are converted into pairs of storage photons (Fig. 1E). Unlike the usual linearly driven dissipative oscillator, which adopts only one oscillation state, our nonlinearly driven dissipative system displays a quantum manifold of SSSs corresponding to all superpositions of two oscillation states with opposite phases.

We used a third mode besides the storage and readout: the excitation of the bridge transmon qubit, restricted to its ground and first excited state. It served as a calibration tool for all of the experimental parameters and as a means to directly measure the Wigner function of the storage. Our system is well described by the effective Hamiltonian for the storage and the readout [(*17*), section 2]

$$\mathbf{H}_{sr}/\hbar = g_2^*\mathbf{a}_s^2\mathbf{a}_r^\dagger + g_2(\mathbf{a}_s^\dagger)^2\mathbf{a}_r + \epsilon_d\mathbf{a}_r^\dagger + \epsilon_d^*\mathbf{a}_r - \chi_{rs}\mathbf{a}_r^\dagger\mathbf{a}_r\mathbf{a}_s^\dagger\mathbf{a}_s - \sum_{m=r,s}\frac{\chi_{mm}}{2}(\mathbf{a}_m^\dagger)^2\mathbf{a}_m^2 \quad (2)$$

The readout and storage annihilation operators are denoted $\mathbf{a}_r$ and $\mathbf{a}_s$, respectively, and $\hbar$ is Planck's constant h divided by 2π. The first four terms constitute a microscopic Hamiltonian of the degenerate parametric oscillator [(*18*), section 9.2.4] with

$$g_2 = \chi_{rs}\xi_p^*/2,$$
$$\xi_p \approx -i\epsilon_p/\left[\frac{\kappa_r}{2} + i(\omega_r - \omega_p)\right]$$

where $\chi_{rs}/2\pi$ = 206 kHz is the dispersive coupling between the readout and the storage, κ_r is the decay rate of the readout, and ϵ_p and ϵ_d are the pump and drive amplitudes, respectively. The terms in g_2 correspond to the conversion of pairs of photons in the storage into single photons in the readout (Fig. 1, D and E). The readout and storage have a Kerr nonlinearity: $\chi_{rr}/2\pi$ = 2.14 MHz and $\chi_{ss}/2\pi$ = 4 kHz, respectively. The Kerr interactions can be considered as perturbations that do not substantially disturb the two-photon conversion effects [(*17*), section 2.3]. The storage and readout single-photon lifetimes are, respectively, $1/\kappa_s$ = 20 μs and $1/\kappa_r$ = 25 ns.

The two-photon processes (Fig. 1, D and E) are activated only when the frequency-matching condition (Eq. 1) is met. We satisfy this condition by performing a calibration experiment (Fig. 2). We excited the readout with a weak continuous wave (CW) probe tone (≈one photon) and measured its transmitted power in the presence of the pump tone while sweeping the frequency of both tones. The pump power is kept fixed during this measurement, and its value was chosen as the largest that did not degrade the coherence times of our system [(*17*), fig. S5]. When the frequency-matching condition is met, the probe photons are converted back and forth into pairs of storage photons (Fig. 1, D and E). When equilibrium is reached for this process, the input probe photons interfere destructively with the back-converted storage photons and are now reflected back into the probe input port [(*18*), section 12.1.1]: the readout is in an induced dark state. The dip (Fig. 2, A and B) is a signature of this interference. Its depth indicates that we have achieved a large nonlinear coupling $g_2 \gg \kappa_s$ [(*17*), section 2.2]. For the subsequent experiments, we fixed the pump frequency to $\omega_p/2\pi$ = 8.011 GHz, which makes the dip coincide with the readout resonance frequency.

We demonstrate that photons are inserted in the storage by measuring the probability of having $n > 0$ photons in the storage while sweeping the readout drive frequency (Fig. 2C). A 10-μs square pulse is applied from the pump and drive tones simultaneously, and then the qubit is excited from its ground to its excited state, conditioned on there being $n = 0$ photons in the storage (*19*). Reading out the qubit state then answers the question of whether there are 0 photons in the storage. The peak at zero detuning shows that the readout drive and the pump combine nonlinearly to insert photons into the storage. The drive tone frequency is chosen such that it maximizes the number of photons in the storage, and the drive power is fixed to ensure an equilibrium average photon number in the storage of about four [(*17*), section 1.4.6].

Adiabatically eliminating the readout from Eq. 2 [(*17*), section 2.3.1; (*18*), section 12.1], we obtain a dynamics for the storage governed by the Hamiltonian

$$\mathbf{H}_s/\hbar = \epsilon_2^*\mathbf{a}_s^2 + \epsilon_2(\mathbf{a}_s^\dagger)^2 - \frac{\chi_{ss}}{2}(\mathbf{a}_s^\dagger)^2\mathbf{a}_s^2$$

and loss operators $\sqrt{\kappa_2}\mathbf{a}_s^2$ and $\sqrt{\kappa_s}\mathbf{a}_s$, where

$$\epsilon_2 = -i\frac{\chi_{sr}}{\kappa_r}\xi_p^*\epsilon_d,\ \kappa_2 = \frac{\chi_{sr}^2}{\kappa_r}|\xi_p|^2$$

The ϵ_2 nonlinear drive inserts pairs of photons in the storage (Fig. 1E) and is analogous to the usual squeezing drive of a nonlinear oscillator [(*14*), equation 1.66]. The novel element in this experiment is the nonlinear decay of rate κ_2, which extracts only photons in pairs from the storage (Fig. 1D). In the absence of unavoidable loss κ_s and neglecting the effect of χ_{ss} [(*17*), section 2.3.2], the storage converges into the two-dimensional (2D) quantum manifold spanned by coherent states $|\pm\alpha_\infty\rangle$, where

$$\alpha_\infty\big|_{\chi_{ss}=\kappa_s=0} = i\sqrt{\frac{2\epsilon_d}{\xi_p\chi_{sr}}}$$

In a classical model where quantum noise is just ordinary noise (*20*), our system behaves as a bistable oscillator with two oscillation states of amplitudes $\pm\alpha_\infty$. The storage then evolves to $+\alpha_\infty$ or $-\alpha_\infty$. However, in the full quantum model, the storage must evolve to $+\alpha_\infty$ and $-\alpha_\infty$ when initialized in the vacuum state, thus forming an even Schrödinger cat state: $\mathcal{N}(|\alpha_\infty\rangle + |-\alpha_\infty\rangle) = \mathcal{N}[\sum_{n=0}^{\infty}(\alpha_\infty^{2n}/2n!)|2n\rangle]$, where $\mathcal{N}$ is a normalization constant (*21*–*25*).

We visualize these dynamics by measuring the state of the storage by direct Wigner tomography (*22*, *26*). The Wigner function [(*27*), section 6.5] is a representation of a quantum state defined over the complex plane as $W(\alpha) = \frac{2}{\pi}\langle\mathbf{D}_\alpha\mathbf{P}\mathbf{D}_{-\alpha}\rangle$, the normalized expectation value of the parity operator $\mathbf{P} = e^{i\pi\mathbf{a}_s^\dagger\mathbf{a}_s}$ for the state displaced by the operator $\mathbf{D}_\alpha = e^{\alpha\mathbf{a}_s^\dagger - \alpha^*\mathbf{a}_s}$. This quasi-probability distribution vividly displays the quantum features of a coherent superposition.

The bistable property of our system is demonstrated by initializing the storage in coherent states with a mean photon number of 6.8 with various phases and observing their convergence to the closest equilibrium state (Fig. 3) (displacement angle = {0, ±π/4, ±3π/4,π}). The upper and lower middle panels (Fig. 3) (displacement angle = ±π/2) correspond to states initialized at almost equal distance from $\pm\alpha_\infty$, which randomly evolve to one equilibrium state or the other, thus converging to the statistical mixture of $\pm\alpha_\infty$.

The coherent splitting of the vacuum into the quantum superposition of $|\pm\alpha_\infty\rangle$ is demonstrated in Fig. 4. In the absence of loss in the storage, the pairwise exchange of photons between the storage and the environment conserves parity. Because the vacuum state is an even-parity state, it must transform into the even cat state: the unique even state contained in the manifold of equilibrium states. Similarly, because Fock state $|1\rangle$ is an odd-parity state, it must transform into the odd cat state [(*17*), fig. S8]. In presence of

κ_s, all coherences will ultimately disappear. However, for large enough κ_2, a quantum superposition transient state is observed.

In this experiment, we achieve $|\xi_p|^2 = 1.2$, which implies $g_2/2\pi$ = 111 kHz and κ_2/κ_s = 1.0. The quantum nature of the transient storage state is visible in the negative fringes of the Wigner function (see Fig. 4, A and B; 7 μs) and the non-Poissonian photon number statistics (Fig. 4D; 7 μs). After 7 μs of pumping, we obtain a state with an average photon number $\overline{n} = 2.4$ and a parity of 42%, which is larger than the parity of a thermal state (17%) or a coherent state (0.8%) with equal $\overline{n}$. After 19 μs of pumping, although the negative fringes vanish, the phase and amplitude of the SSSs $|\pm\alpha_\infty\rangle$ are conserved. Our data are in good agreement with numerical simulations (Fig. 4C), indicating that our dominant source of imperfection is single-photon loss. These results illustrate the confinement of the storage state into the manifold of SSSs and how it transits through a quantum superposition of $|\pm\alpha_\infty\rangle$.

We have realized a nonlinearly driven dissipative oscillator that spontaneously evolves toward the quantum manifold spanned by two coherent states. This was achieved by attaining the regime in which the photon-pair exchange rate is of the same order as the single-photon decay rate. The ratio between these two rates can be further improved within the present technology by using an oscillator with a higher quality factor and increasing the oscillator's nonlinear coupling to the bath. Our experiment is an essential step toward a new paradigm for universal quantum computation (*11*). By combining higher-order forms of our nonlinear dissipation with efficient error syndrome measurements (*28*), quantum information can be encoded and manipulated in a protected manifold of quantum states.

REFERENCES AND NOTES

1. C. Sayrin *et al.*, *Nature* **477**, 73–77 (2011).
2. R. Vijay *et al.*, *Nature* **490**, 77–80 (2012).
3. D. Ristè, C. C. Bultink, K. W. Lehnert, L. DiCarlo, *Phys. Rev. Lett.* **109**, 240502 (2012).
4. P. Campagne-Ibarcq *et al.*, *Phys. Rev. X* **3**, 021008 (2013).
5. H. Krauter *et al.*, *Phys. Rev. Lett.* **107**, 080503 (2011).
6. K. W. Murch *et al.*, *Phys. Rev. Lett.* **109**, 183602 (2012).
7. S. Shankar *et al.*, *Nature* **504**, 419–422 (2013).
8. Y. Lin *et al.*, *Nature* **504**, 415–418 (2013).
9. M. Wolinsky, H. J. Carmichael, *Phys. Rev. Lett.* **60**, 1836–1839 (1988).
10. A. Wallraff *et al.*, *Nature* **431**, 162–167 (2004).
11. M. Mirrahimi *et al.*, *New J. Phys.* **16**, 045014 (2014).
12. G. Kirchmair *et al.*, *Nature* **495**, 205–209 (2013).
13. J. D. Teufel *et al.*, *Nature* **475**, 359–363 (2011).
14. P. Drummond, Z. Ficek, Eds., *Quantum Squeezing* (Series on Atomic, Optical, and Plasma Physics, Springer, Berlin, 2004).
15. I. Siddiqi *et al.*, *Phys. Rev. Lett.* **93**, 207002 (2004).
16. M. A. Castellanos-Beltran, K. D. Irwin, G. C. Hilton, L. R. Vale, K. W. Lehnert, *Nat. Phys.* **4**, 929–931 (2008).
17. See the supplementary materials on *Science* Online for details.
18. H. J. Carmichael, *Statistical Methods in Quantum Optics 2* (Series on Theoretical and Mathematical Physics, Springer, Berlin, 2008).
19. B. Johnson *et al.*, *Nat. Phys.* **6**, 663–667 (2010).
20. M. I. Dykman, M. A. Krivoglaz, *Physica A* **104**, 480–494 (1980).
21. A. Ourjoumtsev, H. Jeong, R. Tualle-Brouri, P. Grangier, *Nature* **448**, 784–786 (2007).
22. B. Vlastakis *et al.*, *Science* **342**, 607–610 (2013).
23. S. Deléglise *et al.*, *Nature* **455**, 510–514 (2008).
24. C. Monroe, D. M. Meekhof, B. E. King, D. J. Wineland, *Science* **272**, 1131–1136 (1996).
25. M. Hofheinz *et al.*, *Nature* **459**, 546–549 (2009).
26. L. G. Lutterbach, L. Davidovich, *Phys. Rev. Lett.* **78**, 2547–2550 (1997).
27. S. Haroche, J.-M. Raimond, *Exploring the Quantum: Atoms, Cavities and Photons* (Oxford Univ. Press, Oxford, 2006).
28. L. Sun *et al.*, *Nature* **511**, 444–448 (2014).
29. D. I. Schuster *et al.*, *Nature* **445**, 515–518 (2007).

ACKNOWLEDGMENTS

We thank L. Jiang and V. V. Albert for helpful discussions. Facilities use was supported by the Yale Institute for Nanoscience and Quantum Engineering and NSF Materials Research Science and Engineering Center Division of Material Research award 1119826. This research was supported by the Army Research Office under grant W911NF-14-1-0011. M.M. acknowledges support from the French Agence Nationale de la Recherche under the project EPOQ2 number ANR-09-JCJC-0070. S.T. acknowledges support from ENS Cachan.

SUPPLEMENTARY MATERIALS

www.sciencemag.org/content/347/6224/853/suppl/DC1
Materials and Methods
Supplementary Text
Figs. S1 to S11
Tables S1 and S2
References (*30*–*37*)

31 October 2014; accepted 22 January 2015
10.1126/science.aaa2085

OPTICS

Spatially structured photons that travel in free space slower than the speed of light

Daniel Giovannini,[1]* Jacquiline Romero,[1]* Václav Potoček,[1,2] Gergely Ferenczi,[1] Fiona Speirits,[1] Stephen M. Barnett,[1] Daniele Faccio,[3] Miles J. Padgett[1]†

That the speed of light in free space is constant is a cornerstone of modern physics. However, light beams have finite transverse size, which leads to a modification of their wave vectors resulting in a change to their phase and group velocities. We study the group velocity of single photons by measuring a change in their arrival time that results from changing the beam's transverse spatial structure. Using time-correlated photon pairs, we show a reduction in the group velocity of photons in both a Bessel beam and photons in a focused Gaussian beam. In both cases, the delay is several micrometers over a propagation distance of ~1 meter. Our work highlights that, even in free space, the invariance of the speed of light only applies to plane waves.

The speed of light is trivially given as c/n, where c is the speed of light in free space and n is the refractive index of the medium. In free space, where n = 1, the speed of light is simply c. We show that the introduction of transverse structure to the light beam reduces the group velocity by an amount that depends on the aperture of the optical system. The delay corresponding to this reduction in the group velocity can be greater than the optical wavelength and consequently should not be confused with the ≈π Gouy phase shift (*1*, *2*). To emphasize that this effect is both a linear and intrinsic property of light, we measure the delay as a function of the transverse spatial structure of single photons.

The slowing down of light that we observe in free space should also not be confused with slow, or indeed fast, light associated with propagation in highly nonlinear or structured materials (*3*, *4*). Even in the absence of a medium, the modification of the speed of light has previously been known. For example, within a hollow waveguide, the wave vector along the guide is reduced below the free-space value, leading to a phase velocity v_ϕ greater than c. Within the hollow waveguide, the product of the phase and group velocities is given as $v_\phi v_{g,z} = c^2$, thereby resulting in a group velocity $v_{g,z}$ along the waveguide less than c (*5*).

Although this relation for group and phase velocities is derived for the case of a hollow waveguide, the waveguide material properties are irrelevant. It is the transverse spatial confinement of the field that leads to a modification of the axial component of the wave vector, k_z. In general, for light of wavelength λ, the magnitude of the wave vector, $k_0 = 2\pi/\lambda$, and its Cartesian components $\{k_x, k_y, k_z\}$ are related through (*5*)

$$k_z^2 + k_x^2 + k_y^2 = k_0^2$$

All optical modes of finite x,y spatial extent require nonzero k_x and k_y, which implies $k_z < k_0$, giving a corresponding modification of both the phase and group velocities of the light. In this sense, light beams with nonzero k_x and k_y are naturally dispersive, even in free space.

Extending upon the case of a mode within a hollow waveguide, an example of a structured

[1]School of Physics and Astronomy, Scottish Universities Physics Alliance (SUPA), University of Glasgow, Glasgow G12 8QQ, UK. [2]Faculty of Nuclear Sciences and Physical Engineering, Czech Technical University in Prague, Břehová 7, 115 19 Praha 1, Czech Republic. [3]School of Engineering and Physical Sciences, SUPA, Heriot-Watt University, Edinburgh EH14 4AS, UK.
*These authors contributed equally to this work. †Corresponding author. E-mail: miles.padgett@glasgow.ac.uk